Full-dimensional quantum dynamics study on the mode-specific unimolecular dissociation reaction of HFCO

Takeshi Yamamoto and Shigeki Kato[a]
Department of Chemistry, Graduate School of Science, Kyoto University, Kitashirakawa, Sakyo-ku, Kyoto 606-8502, Japan

The mode specificity of the unimolecular reaction of HFCO is studied by six-dimensional quantum dynamics calculations. The energy and mode dependency of the dissociation rate is examined by propagating a number of wave packets with a small energy dispersion representing highly excited states with respect to a specific vibrational mode. The wave packets are generated by applying a set of filter operators onto a source vibrational state. All the information necessary for propagating the wave packets is obtained from a single propagation of the source state, thus allowing a significant decrease of computational effort. The relevant spectral peaks are assigned using the three-dimensional CH chromophore Hamiltonian. The resulting dissociation rate of the CH stretching excited state is in agreement with that obtained from a statistical theory, while the rates of the out-of-plane bending excited states are about one order of magnitude smaller than the statistical rates. A local-mode analysis also shows that the relaxation of the out-of-plane excitation proceeds very slowly within 3 ps. These results clearly indicate weak couplings of the out-of-plane bending excited states with other in-plane vibrational states, which is in qualitative agreement with experimental findings. From a computational point of view, a parallel supercomputer is utilized efficiently to handle an ultra large basis set of an order of 10^8, and 200 Gflops rate on average is achieved in the dynamics calculations. © *2000 American Institute of Physics.* [S0021-9606(00)00918-1]

I. INTRODUCTION

In recent years, accurate quantum dynamics calculations have been performed for a variety of small polyatomic systems including three- and four-atom molecules as well as van der Waals clusters.[1,2] Those rigorous treatments of gas-phase reactions are of fundamental importance, not only because they can provide information on the underlying dynamics and associated quantities from the first-principle calculations, but also the comparison of computational results with experimental ones enables us to assess the reliability of available potential surfaces. Another important aspect of those calculations is the role as a benchmark for more approximate treatments such as trajectory-based propagation methods[3-7] or multi-configurational time-dependent Hartree approaches.[8] However, the computational cost required for rigorous quantum dynamics calculations increases exponentially with basis set size, thus the application to a larger system becomes more difficult. In fact, rigorous treatments of four-atom systems involving heavy atoms and/or with large total energy still present a challenge for theoretical chemists.

In the present paper we study the dissociation dynamics of the highly vibrationally excited states of formyl fluoride, HFCO, on the ground S_0 potential surface,

$$HFCO \rightarrow HF + CO \qquad (1)$$

by performing full-dimensional quantum dynamics calcula-tions. This reaction has received considerable attention because of its mode-specific behavior observed in the stimulated emission pumping (SEP) experiments by Choi and Moore.[9] In their experiments, highly vibrationally excited HFCO is generated on the S_0 surface, and particularly the out-of-plane bending mode undergoes extremely high excitation. The striking feature observed in the SEP spectra is that the highly excited states with respect to the out-of-plane bending mode, the so-called ''extreme-motion'' states, suffer nearly no state mixing with other in-plane vibrational states, and it was found that this nature becomes more evident as the total energy is increased. On the other hand, Crane *et al.*[10] recently carried out similar SEP experiments on DFCO and reported that the stability of the extreme-motion states is destroyed in the case of DFCO. This was attributed to the greatly enhanced resonances between the out-of-plane bending and CO stretching modes due to the change of their vibrational frequencies.

Theoretically, HFCO has long been the subject of *ab initio* quantum chemical studies, in which various reaction pathways and their barrier heights have been estimated.[11-15] Global analytical fits of the S_0 potential surface were obtained by Wei and Wyatt[16] and by the present authors,[17] both of which are capable of describing the dissociation channel (1). Budenholzer and Yu[18] performed a classical trajectory calculation for this reaction using a modified version of the potential surface by Wei and Wyatt, and found strong mode specificity in the dissociation rate depending on the initial distribution of the vibrational energy. They concluded that

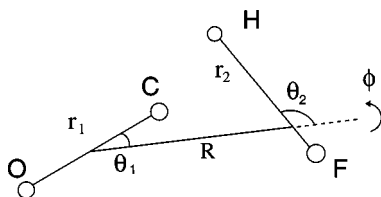[a]Electronic mail: shigeki@kuchem.kyoto-u.ac.jp

     8006

FIG. 1. The diatom–diatom Jacobi coordinates used in the dynamics calculations.

the CH stretching or bending excitation greatly enhance the dissociation rate, while the out-of-plane or CO stretching excitation results in a significantly slower dissociation. Very recently, Viel and Leforestier[19] have performed a quantum mechanical calculation of vibrational eigenstates at the relatively low energy region using the adiabatic pseudospectral (APS) method,[20] and have tested the accuracy of the two analytical potential surfaces.

In a previous work,[21] we carried out planar four-dimensional (4D) and five-dimensional (5D) quantum dynamics calculations of the reaction (1), where we examined dependency of the dissociation rate on vibrational character or total energy of the initial state. Specifically, we generated several initial states with different distribution of vibrational energy and compared the dissociation rates by propagating them in time independently. The resulting time-dependent rates showed a rapid convergence to the same asymptotic value with a small fluctuation, which indicated that the intramolecular vibrational energy redistribution (IVR) above the dissociation threshold was considerably fast in the planar model. This observation was also confirmed by directly monitoring the time variation of the local-mode energies.

In the present paper we incorporate the out-of-plane degree of freedom into the dynamics calculations. This allows us to compare the dissociation rates from the out-of-plane extreme-motion states with those from other in-plane vibrational states such as the CH stretch overtone states. For this purpose we adopt basically the same approach as in the previous work,[21] but a new technique is introduced to reduce the computational effort drastically; i.e., energy dependency of the dissociation rate is estimated from a single wave packet propagation. It should be noted here that the present rate describes the dissociation rate of a locally excited wave packet instead of the statistically averaged rate at a given total energy, which permits us to study the mode dependency of the dissociation rates.

This paper is organized as follows: in Sec. II we describe the theoretical framework for calculating the dissociation rates of locally excited filter states. In Sec. III we present the assignment of spectral peaks using a three-dimensional CH chromophore Hamiltonian and discuss the obtained decay rates of the out-of-plane bending or CH stretching excited states. In Sec. IV we conclude.

II. METHOD

A. Hamiltonian and basis set

The Hamiltonian describing the dissociation dynamics is written using diatom–diatom Jacobi coordinates in Fig. 1 as

follows (atomic units $\hbar=1$ is used):[22]

$$\hat{H}=-\frac{1}{2\mu_1}\frac{\partial^2}{\partial r_1^2}-\frac{1}{2\mu_2}\frac{\partial^2}{\partial r_2^2}-\frac{1}{2\mu}\frac{\partial^2}{\partial R^2}-\frac{1}{2I_1(r_1,R)}\hat{D}(\theta_1)$$
$$-\frac{1}{2I_2(r_2,R)}\hat{D}(\theta_2)-\frac{1}{2I(r_1,r_2,R,\theta_1,\theta_2)}\hat{D}(\phi)$$
$$+\hat{T}_{\mathrm{cross}}+V(r_1,r_2,R,\theta_1,\theta_2,\phi), \tag{2}$$

where μ_1, μ_2, and μ are the reduced masses associated with r_1, r_2, and R, respectively, while the effective inertia moments I_1, I_2, and I are given as

$$\frac{1}{I_1(r_1,R)}=\frac{1}{\mu_1 r_1^2}+\frac{1}{\mu R^2},$$

$$\frac{1}{I_2(r_2,R)}=\frac{1}{\mu_2 r_2^2}+\frac{1}{\mu R^2}, \tag{3}$$

$$\frac{1}{I(r_1,r_2,R,\theta_1,\theta_2)}=\frac{1}{I_1(r_1,R)\sin^2\theta_1}+\frac{1}{I_2(r_2,R)\sin^2\theta_2}$$
$$-\frac{2}{\mu R^2}.$$

The cross term $\hat{T}_{\mathrm{cross}}$ in Eq. (2) is of the form

$$\hat{T}_{\mathrm{cross}}=\frac{1}{\mu R^2}\{-\cos\phi\hat{F}(\theta_1)\hat{F}(\theta_2)+(\cot\theta_1\hat{F}(\theta_2)$$
$$+\cot\theta_2\hat{F}(\theta_1))\hat{F}(\phi)+\cot\theta_1\cot\theta_2\hat{G}(\phi)\}, \tag{4}$$

and one-dimensional operators in Eqs. (2) and (4) are defined as

$$\hat{D}(\theta_k)=\frac{1}{\sin\theta_k}\frac{\partial}{\partial\theta_k}\sin\theta_k\frac{\partial}{\partial\theta_k} \quad (k=1,2),$$

$$\hat{D}(\phi)=\frac{\partial^2}{\partial\phi^2},$$

$$\hat{F}(\theta_k)=\frac{\partial}{\partial\theta_k}+\frac{1}{2}\cot\theta_k \quad (k=1,2), \tag{5}$$

$$\hat{F}(\phi)=\sin\phi\frac{\partial}{\partial\phi}+\frac{1}{2}\cos\phi,$$

$$\hat{G}(\phi)=\cos\phi\frac{\partial^2}{\partial\phi^2}-\sin\phi\frac{\partial}{\partial\phi}-\frac{1}{4}\cos\phi.$$

In this paper we consider the dissociation dynamics for total angular momentum $J=0$ with A' vibrational symmetry, and thus the basis set for ϕ is restricted to even functions.

As for the potential term V in Eq. (2) we employ the global analytical function constructed by the present authors,[17] which was obtained by fitting to a large number of *ab initio* potential energies computed at the level of Hartree–Fock plus second-order Møller–Plesset perturbation theory. This potential surface has a deep well representing HFCO, and the classical barrier height for the reaction (1) is 51.2 kcal/mol. The zero of potential energy is taken at the equilibrium geometry of HFCO throughout this paper.

As basis sets for representing a six-dimensional wave function, we adopt the potential optimized discrete variable representation (PODVR)[23] for all the Jacobi coordinates except for R, and the latter coordinate is represented by using the sinc-DVR.[24] (This exceptional treatment of R is related to a parallelization issue described below.) In order to set up the PODVR basis we first obtain the eigenstates of the following 1D reference Hamiltonian $\hat{h}_k$ for each coordinate x_k:

$$\hat{h}_1 = -\frac{1}{2\mu_1}\frac{\partial^2}{\partial r_1^2} + v_1(r_1),$$

$$\hat{h}_2 = -\frac{1}{2\mu_2}\frac{\partial^2}{\partial r_2^2} + v_2(r_2),$$

$$\hat{h}_4 = -\frac{1}{2\bar{I}_1}\hat{D}(\theta_1) + v_4(\theta_1), \tag{6}$$

$$\hat{h}_5 = -\frac{1}{2\bar{I}_2}\hat{D}(\theta_2) + v_5(\theta_2),$$

$$\hat{h}_6 = -\frac{1}{2\bar{I}}\hat{D}(\phi) + v_6(\phi),$$

where $\bar{I}_1$, $\bar{I}_2$, and $\bar{I}$ are the inertia moments in Eq. (3) at the equilibrium geometry of HFCO, and $v_k(x_k)$ represents a 1D reference potential function. We then select the lowest n_k eigenstates of $\hat{h}_k$, diagonalize an appropriate coordinate operator within the chosen eigenstates, and finally obtain the PODVR basis as a linear combination of the eigenstates. Note here that the PODVR basis functions thus obtained are localized around the associated eigenvalues of the coordinate matrix, and these eigenvalues (called the PODVR grid points) are distributed semiclassically; i.e., the density of the PODVR points becomes larger where the reference potential is deeper. We can take advantage of this fact in order to generate a compact multidimensional basis set adaptive to the global potential features. This is achieved by appropriately defining the reference potential in Eq. (6), and in practice we choose $v_k(x_k)$ as a minimum energy curve along x_k:

$$v_k(x_k) = \min_{\text{all } x_j(j \neq k)} V(\mathbf{x}), \tag{7}$$

where $\mathbf{x}$ denotes $(r_1, r_2, R, \theta_1, \theta_2, \phi)$ and $V(\mathbf{x})$ stands for the global potential function. With this definition $v_2(r_2)$ becomes a double-well potential which runs through the interaction zone as well as the product valley. It is also noted that the sum of the reference potentials, $\Sigma v_k(x_k)$, can be regarded as a zeroth-order approximation to the global potential function.

A six-dimensional wave function is constructed as the sum of direct products of one-dimensional bases as

$$|\Psi\rangle = \sum_I C_I |i_{r_1}\rangle |i_{r_2}\rangle |i_R\rangle |i_{\theta_1}\rangle |i_{\theta_2}\rangle |i_\phi\rangle, \tag{8}$$

where I denotes the six indices collectively. $|i_R\rangle$ represents the sinc-DVR basis while the others are the PODVR bases defined above. When applying the total Hamiltonian onto the six-dimensional wave function, we first rewrite the Hamiltonian as

$$\hat{H} = -\frac{1}{2\mu}\frac{\partial^2}{\partial R^2} + \sum_{k(\neq 3)}\hat{h}_k$$
$$+ \frac{1}{2}\left(\frac{1}{\bar{I}_1} - \frac{1}{I_1(r_1,R)}\right)\hat{D}(\theta_1) + \frac{1}{2}\left(\frac{1}{\bar{I}_2} - \frac{1}{I_2(r_2,R)}\right)\hat{D}(\theta_2)$$
$$+ \frac{1}{2}\left(\frac{1}{\bar{I}} - \frac{1}{I(r_1,r_2,R,\theta_1,\theta_2)}\right)\hat{D}(\phi) + \hat{T}_{\text{cross}} + V_{\text{eff}}(\mathbf{x}),$$
$$\tag{9}$$

where $V_{\text{eff}}(\mathbf{x})$ is the global effective potential,

$$V_{\text{eff}}(\mathbf{x}) = V(\mathbf{x}) - \sum_{k(\neq 3)} v_k(x_k). \tag{10}$$

The matrix representation of the total Hamiltonian is composed of exact small matrices for the 1D operators in Eq. (5) and the multiplicative factors approximated as diagonal within the DVR scheme. The overall Hermiticity of the Hamiltonian matrix is automatically ensured since all the 1D operators in Eq. (5) are Hermitian or anti-Hermitian.[22] Although the diagonal approximation applied to the multiplicative factors causes a loss of accuracy, the error associated with the global potential term can be significantly reduced by subtracting the sum of reference potentials from the global potential as in Eq. (10). This reduction of error probably comes from the decreased magnitude and curvature of the effective potential $V_{\text{eff}}(\mathbf{x})$ compared to the original potential $V(\mathbf{x})$. In other words, zeroth-order variation of the global potential surface is incorporated in the 1D reference Hamiltonians $\hat{h}_k$ in Eq. (9). We notice that the above reordering of operators as well as the definition of the PODVR basis is analogous to those used in a recent quantum mechanical study of a HOCl molecule.[25]

B. Propagation of the filter states

In order to examine the mode specificity of the out-of-plane extreme-motion states observed in experiments, we compare the dissociation rates initiated from two different types of highly vibrationally excited states, that is, states with high excitation in the out-of-plane bending mode or in-plane CH stretching mode. For this purpose we adopt a semiquantitative approach that is an extension of our previous work;[21] i.e., instead of computing the individual molecular eigenstates, we examine the time evolution of a wave packet with a relatively small energy dispersion and specific vibrational character.

First, we generate a ''source'' vibrational state Φ that is characterized by excitation of a single vibrational mode by the method described in the next subsection. Roughly speaking, this state corresponds to a superposition of several eigenstates of a conveniently chosen zeroth-order Hamiltonian. Although this source state has a clear vibrational character, its time evolution does not directly provide useful information since this state includes a number of molecular eigenstates with various total energies. In order to extract information on the dynamics associated with each total energy, we apply a spectral filter $\hat{F}(E)$ with a window energy E to the source vibrational state Φ, thus generating a filter state

$\Psi(E)$ that has a relatively small energy dispersion, i.e., $\Psi(E) = \hat{F}(E)\Phi$. Our basic strategy for studying the energy and mode dependency of the dissociation rate consists in propagating a set of filter states $\{\Psi(E)\}$ with various window energies and source states,

$$\Psi(t|E) = \hat{U}(t)[\hat{F}(E)\Phi], \tag{11}$$

and then analyzing the individual wave packets $\{\Psi(t|E)\}$ thus obtained. Here $\hat{U}(t)$ denotes the time evolution operator under the absorbing boundary condition (ABC).[26]

In the previous work,[21] several filter states with different window energies were explicitly generated and propagated in time independently. (For instance, four filter states were propagated independently to examine the CH stretch overtone states with $v = 5, 6, 7,$ and 8.) An obvious disadvantage of such a method is that the necessary computational effort increases proportionally to the number of window energies of interest, which makes it quite expensive to analyze the energy dependence of dynamics.

We find that this computational inefficiency can be overcome by defining the filter operator as

$$\hat{F}_{T_0}(E) = \int_0^{T_0} dt \; e^{iEt} \; \hat{U}(t). \tag{12}$$

When we write the ABC Hamiltonian[26] as $\hat{H}_c := \hat{H} - i\hat{W}$ with $\hat{W}$ being an absorbing potential, this filter operator can be integrated using $\hat{U}(t) = \exp(-i\hat{H}_c t)$ as

$$\hat{F}_{T_0}(E) = \frac{\exp\{i(E - \hat{H}_c)T_0\} - 1}{i(E - \hat{H}_c)}, \tag{13}$$

hence it converges to the ABC Green's function $i\hat{G}(E) = i(E - \hat{H}_c)^{-1}$ when T_0 goes to infinity. Now suppose that a set of filter states $\{\Psi(t|E_k)\}$ with different window energies $\{E_k\}$ are generated as $\{\hat{F}_{T_0}(E_k)\Phi\}$, and that they are propagated in time as

$$\Psi(t|E_k) = \hat{U}(t)[\hat{F}_{T_0}(E_k)\Phi]. \tag{14}$$

The first key to an efficient calculation is that the time propagator and filter operator commute with each other:

$$[\hat{U}(t), \hat{F}_{T_0}(E_k)] = \left[\hat{U}(t), \int_0^{T_0} dt' \, e^{iE_k t'} \hat{U}(t')\right]$$

$$= \int_0^{T_0} dt' \, e^{iE_k t'} [\hat{U}(t), \hat{U}(t')] = 0, \tag{15}$$

where we have used the fact that the two ABC propagators $\hat{U}(t)$ and $\hat{U}(t')$ commute as long as both t and t' are positive. Then, we can exchange the order of these operators in Eq. (14) as

$$\Psi(t|E_k) = \hat{F}_{T_0}(E_k)\hat{U}(t)\Phi = \hat{F}_{T_0}(E_k)\Phi(t). \tag{16}$$

Therefore, $\Psi(t|E_k)$ can be obtained by first propagating Φ up to a time t and then applying the filter $\hat{F}_{T_0}(E_k)$ onto the propagated source state $\Phi(t)$.

The second point is to propagate the source state $\Phi(t)$ by every T_0 time step. To be specific, let us expand the time propagator $\hat{U}(t)$ for $0 < t < T_0$ in terms of the modified Chebyshev polynomials:[1,27]

$$\hat{U}(t) = \sum_{n=0}^{N_H} a_n(t)Q_n(\hat{H}_{\text{norm}}; \hat{\gamma}) \quad (0 < t < T_0), \tag{17}$$

where the expansion coefficients are given as

$$a_n(t) = \frac{2 - \delta_{n,0}}{\pi} \int_0^\pi d\theta \cos(n\theta)\exp\{-i(\bar{H} + \Delta H \cos\theta)t\}. \tag{18}$$

Here $\hat{H}_{\text{norm}}$ refers to a scaled Hamiltonian, $\hat{H}_{\text{norm}} = (\hat{H} - \bar{H})/\Delta H$, with $\bar{H} = (H_{\max} + H_{\min})/2$ and $\Delta H = (H_{\max} - H_{\min})/2$, and $H_{\max}$ and $H_{\min}$ are the estimates of the maximum and minimum eigenvalues of the total Hamiltonian, respectively. The modified Chebyshev polynomials $Q_n(\hat{H}_{\text{norm}}; \hat{\gamma})$ are defined by the following recurrence relations:

$$Q_0(\hat{H}_{\text{norm}}; \hat{\gamma}) = \hat{I},$$

$$Q_1(\hat{H}_{\text{norm}}; \hat{\gamma}) = e^{-\hat{\gamma}}\hat{H}_{\text{norm}}, \tag{19}$$

$$Q_n(\hat{H}_{\text{norm}}; \hat{\gamma}) = e^{-\hat{\gamma}}2\hat{H}_{\text{norm}}Q_{n-1}(\hat{H}_{\text{norm}}; \hat{\gamma})$$
$$- e^{-2\hat{\gamma}}Q_{n-2}(\hat{H}_{\text{norm}}; \hat{\gamma}),$$

where $e^{-\hat{\gamma}}$ represents a damping function that enforces the absorbing boundary condition. By substituting the expansion of $\hat{U}(t)$ in Eq. (17) into the definition of the filter operator in Eq. (12), we can see that $\hat{F}_{T_0}(E)$ can also be expanded in terms of the same polynomials as

$$\hat{F}_{T_0}(E) = \sum_{n=0}^{N_H} b_n(E)Q_n(\hat{H}_{\text{norm}}; \hat{\gamma}), \tag{20}$$

with the coefficients $b_n(E)$ written as

$$b_n(E) = \int_0^{T_0} dt \; e^{iEt}a_n(t), \tag{21}$$

or using an integral form of $a_n(t)$ in Eq. (18) as

$$b_n(E) = \frac{2 - \delta_{n,0}}{\pi} \int_0^\pi d\theta \cos(n\theta)$$

$$\times \frac{\exp\{i(E - (\bar{H} + \Delta H \cos\theta)\} - 1}{i\{E - (\bar{H} + \Delta H \cos\theta)\}}. \tag{22}$$

Equations (18) and (22) are suited for accurate numerical evaluation using high-order Gauss–Chebyshev quadrature.[28]

Combining Eqs. (17) and (20), we find that if $\Phi(mT_0)$ is already known, both $\Phi((m+1)T_0)$ and $\{\Psi(mT_0|E_k)\}$ with arbitrary energies $\{E_k\}$ can be simultaneously obtained by generating $\{Q_n(\hat{H}_{\text{norm}}; \hat{\gamma})\Phi(mT_0)\}$ recursively up to N_H terms:

$$\Phi((m+1)T_0) = \sum_{n=0}^{N_H} a_n(T_0)Q_n(\hat{H}_{\text{norm}}; \hat{\gamma})\Phi(mT_0), \tag{23}$$

$$\Psi(mT_0|E_k)=\sum_{n=0}^{N_H} b_n(E_k)Q_n(\hat{H}_{\text{norm}};\hat{\gamma})\Phi(mT_0). \quad (24)$$

In addition, the autocorrelation function of the source state at an arbitrary time mT_0+t' for $0<t'<T_0$ is obtained using Eq. (17) as

$$C(mT_0+t')=\langle\Phi|\Phi(mT_0+t')\rangle$$
$$=\sum_{n=0}^{N_H} a_n(t')\langle\Phi|Q_n(\hat{H}_{\text{norm}};\hat{\gamma})\Phi(mT_0)\rangle.$$
$$(25)$$

Hence, this scheme provides the source vibrational state $\Phi(t)$ and a set of filter states $\{\Psi(t|E_k)\}$ at discrete times, $t=mT_0(m=0,1,2,...)$, along with the autocorrelation function of the source state $C(t)$ at an arbitrary time. We emphasize that no extra computational cost is required for the filter operation itself in the practical implementation; i.e., the net computational effort is only for a single propagation of the source vibrational state, $\Phi(t)$. Another advantage of this scheme is that the efficiency of the Chebyshev expansion in Eq. (17) becomes nearly optimal, since we take T_0 considerably long ($\sim$100 fs) and the resulting expansion order N_H becomes as large as 3000.

C. Source vibrational states

As the source vibrational states Φ mentioned above, we consider two types of states that are highly excited in the out-of-plane bending mode or CH stretching mode, which are denoted as Φ_{OP} and Φ_{CH}, respectively.

First, we define Φ_{OP} as a direct product of one-dimensional vibrational functions as follows:

$$\Phi_{\text{OP}}=N\left(\sum_n \varphi_n^{(6)}(\phi)\right)\prod_{k=1}^{5}\varphi_0^{(k)}(x_k), \quad (26)$$

where N is the normalization constant while $\varphi_n^{(k)}(x_k)$ represents the nth eigenstate of a one-dimensional Hamiltonian $\hat{h}_k^{\text{dia}}$ describing diabatic motion associated with each Jacobi coordinate x_k, that is,

$$\hat{h}_k^{\text{dia}}\varphi_n^{(k)}(x_k)=\epsilon_n^{(k)}\varphi_n^{(k)}(x_k). \quad (27)$$

The 1D Hamiltonian $\hat{h}_k^{\text{dia}}$ is defined in the same manner as the 1D reference Hamiltonian in Eq. (6), but the potential term is replaced with a 1D diabatic potential, $v_k^{\text{dia}}(x_k)$, which is defined by fixing all other Jacobi coordinates except for x_k at their equilibrium values of HFCO in the 6D potential function $V(\mathbf{x})$. Roughly speaking, $\hat{h}_k^{\text{dia}}$ can be regarded as a local-mode Hamiltonian describing a local vibration associated with x_k, and hence Φ_{OP} represents a state where the out-of-plane bending mode, which is approximately identified as ϕ, is highly excited while the other local modes are constrained to their zero-point vibrations. It may be worth noting that these definitions are not intended to provide a spectroscopically observable local-mode states, and as a re-

sult, the quantum number n in Eq. (26) does not correspond to a spectroscopically assigned quantum number. The issue concerning the assignment of extreme-motion states will be discussed in Sec. III.

In contrast to the out-of-plane case described above, it is not straightforward to generate the CH stretching excited state, Φ_{CH}, since no single Jacobi coordinate can describe the CH stretching motion. We circumvent this problem by employing the following sequential steps; i.e., we first generate such a state in a bond coordinate system and then transform the resulting wave function into the Jacobi coordinate representation.

In the first step, the CH stretching excited state $\Phi_{\text{CH}}^{\text{B}}$ is defined using the Bond coordinates $\mathbf{x}^{\text{B}}=(r_{\text{CH}},r_{\text{CF}},r_{\text{CO}},\theta_{\text{HCO}},\theta_{\text{FCO}},\phi_{\text{B}})$ as

$$\Phi_{\text{CH}}^{\text{B}}=N\left(\sum_n \varphi_n^{(1),\text{B}}(r_{\text{CH}})\right)\prod_{k=2}^{6}\varphi_0^{(k),\text{B}}(x_k^{\text{B}}), \quad (28)$$

where $\{\varphi_n^{(k),\text{B}}(x_k^{\text{B}})\}$ are eigenfunctions of the following 1D local-mode Hamiltonians:

$$\hat{h}_k^{\text{dia,B}}(r_{\text{CX}})=-\frac{1}{2\mu_{\text{CX}}}\frac{\partial^2}{\partial r_{\text{CX}}^2}+v_k^{\text{dia,B}}(r_{\text{CX}})$$
$$(\text{X=H,F,O}\quad\text{for }k=1,2,3),$$

$$\hat{h}_k^{\text{dia,B}}(\theta_{\text{XCO}})=-\frac{1}{2I_{\text{XCO}}}\frac{1}{\sin\theta_{\text{XCO}}}\frac{\partial}{\partial\theta_{\text{XCO}}}\sin\theta_{\text{XCO}}\frac{\partial}{\partial\theta_{\text{XCO}}}$$
$$+v_k^{\text{dia,B}}(\theta_{\text{XCO}})\quad(\text{X=H,F}\quad\text{for }k=4,5),$$
$$(29)$$

$$\hat{h}_6^{\text{dia,B}}(\phi_{\text{B}})=-\frac{1}{2I_{\text{OP}}}\frac{\partial^2}{\partial\phi_{\text{B}}^2}+v_6^{\text{dia,B}}(\phi_{\text{B}}),$$

with the reduced masses and inertia moments as

$$\frac{1}{\mu_{\text{CX}}}=\frac{1}{M_{\text{C}}}+\frac{1}{M_{\text{X}}}\quad(\text{X=H,F,O}),$$

$$\frac{1}{I_{\text{XCO}}}=\frac{1}{\mu_{\text{CX}}\bar{r}_{\text{CX}}^2}+\frac{1}{\mu_{\text{CO}}\bar{r}_{\text{CO}}^2}\quad(\text{X=H,F}), \quad (30)$$

$$\frac{1}{I_{\text{OP}}}=\frac{1}{I_{\text{HCO}}\sin^2\bar{\theta}_{\text{HCO}}}+\frac{1}{I_{\text{FCO}}\sin^2\bar{\theta}_{\text{FCO}}}-\frac{2}{\mu_{\text{CO}}\bar{r}_{\text{CO}}^2},$$

where M_{X} denotes the mass of atom X. These definitions are based on the diagonal parts of the full-dimensional kinetic operator in the bond coordinates.[29] Note that we distinguish quantities associated with the Bond and Jacobi coordinates by superscripts B and J, respectively.

In the second step, we transform $\Phi_{\text{CH}}^{\text{B}}$ in Eq. (28) into that in the Jacobi coordinate representation, $\Phi_{\text{CH}}^{\text{J}}$. By imposing the conservation of probability density as

$$|\Phi_{\text{CH}}^{\text{J}}|^2\sin\theta_1\sin\theta_2 d\mathbf{x}^{\text{J}}=|\Phi_{\text{CH}}^{\text{B}}|^2\sin\theta_{\text{HCO}}\sin\theta_{\text{FCO}}d\mathbf{x}^{\text{B}}, \quad (31)$$

and also using the coordinate transformation rule as

TABLE I. The number of basis functions. The PODVR is used for all the Jacobi coordinates except for R, while the sinc-DVR is employed for R. Minimum and maximum values of the grids are listed in Å and degrees. The basis functions of ϕ are restricted to even functions.

x	n	x_{min}	x_{max}
r_1	7	1.08	1.35
r_2	25	0.76	2.93
R	80	1.30	2.90
θ_1	39	9.1	97.5
θ_2	20	98.6	151.9
ϕ	14	-62.7	62.7

$$dx^B = \left| \frac{\partial x^B}{\partial x^J} \right| dx^J, \tag{32}$$

we can express Φ_{CH}^J as a product of Φ_{CH}^B and an appropriate correction factor as follows:

$$\Phi_{CH}^J = \Phi_{CH}^B \left\{ \frac{\sin \theta_{HCO} \sin \theta_{FCO}}{\sin \theta_1 \sin \theta_2} \left| \frac{\partial x^B}{\partial x^J} \right| \right\}^{1/2}. \tag{33}$$

The actual implementation of Eq. (33) requires first transforming all the Jacobi coordinates on the grid points into the bond coordinates and then interpolating the functional values of Φ_{CH}^B at the obtained bond coordinates. Since Φ_{CH}^B is written as a direct product of 1D functions as in Eq. (28), the interpolation can be easily and accurately carried out, and thus the overall transformation is not computationally demanding. In addition, the PODVR basis functions in the Jacobi coordinates have an interpolating nature similar to that of the DVR based on the Gaussian quadrature, and this fact is fully utilized in the transformation step.

D. Computational details

As mentioned above we use the sinc-DVR for the scattering coordinate R and the PODVR for the other Jacobi coordinates. As a primitive basis for obtaining the eigenstates of the 1D reference Hamiltonians in Eq. (6), we employ the sinc-DVR for r_1 and r_2, first-order associated Legendre functions for θ_1 and θ_2, and cosine functions for ϕ, respectively. The following coordinate operators, i.e., r_1, r_2, $\cos \theta_1$, $\cos \theta_2$, and $\cos \phi$, are then diagonalized using the lowest n_k eigenstates of $\hat{h}_k$, respectively. The number of PODVR basis along with the minimum and maximum values of the PODVR grid points are listed in Table I. Although the resulting direct product basis set is not truncated and the number of the whole basis becomes as large as 1.5×10^8, this huge basis set is handled efficiently by using a parallel supercomputer as described below. The damping function $e^{-\hat{\gamma}}$ in the Chebyshev recursion formula in Eq. (19) is defined simply as $\exp[-((R-R_{abs})/\Delta R_{abs})^2]$ for $R>R_{abs}$ and 1 otherwise with $R_{abs}=2.7$ Å and $\Delta R_{abs}=0.1$ Å.

As is often the case, the central task of the present calculation consists of a large number of repeated operations of the Hamiltonian onto a vector. Therefore, from a computational point of view it is important not only to reduce the total number of the Hamiltonian operations but to minimize the CPU time required for a single operation step.

For the first issue we must take into account the fact that the number of the Hamiltonian operations needed for a fixed-time propagation via Eq. (17) increases proportionally to the spectral range of the Hamiltonian. As such, reducing the spectral range directly leads to a saving of computational effort. For the present Hamiltonian in Eq. (9), we find that the term

$$\frac{1}{2} \left(\frac{1}{\bar{\bar{I}}} - \frac{1}{I(r_1, r_2, R, \theta_1, \theta_2)} \right) \hat{D}(\phi), \tag{34}$$

enlarges the spectral range most significantly, where the largest eigenvalues of the term arise from combinations of the smallest values of the inertia moment and the largest negative eigenvalues of $\hat{D}(\phi)$. Since we can expect that components with too high eigenvalues would be irrelevant in describing the dynamics, we cut off such components by replacing the term in Eq. (34) with the following:

$$\sum_n |d_n\rangle g\left[\frac{1}{2} \left(\frac{1}{\bar{\bar{I}}} - \frac{1}{I(r_1, r_2, R, \theta_1, \theta_2)} \right) d_n; E_{cut} \right] \langle d_n|, \tag{35}$$

where d_n and $|d_n\rangle$ are eigenvalues and eigenvectors of $\hat{D}(\phi)$, respectively, while the cutoff function $g[E; E_{cut}]$ is chosen as E for $E < E_{cut}$ and E_{cut} otherwise. Within the DVR scheme, eigenstates of the term in Eq. (34) are given simply as

$$|I', n\rangle = |i_{r_1}\rangle |i_{r_2}\rangle |i_R\rangle |i_{\theta_1}\rangle |i_{\theta_2}\rangle |d_n\rangle, \tag{36}$$

where I' stands for the five indices for DVR bases and we denote the associated eigenenergies as $E[I', n]$. The modification in Eq. (35) is justified if the following sum of populations of these eigenstates,

$$\sum_{I', n} |\langle I', n | \Psi(t) \rangle|^2 \quad (E[I', n] > E_{cut}), \tag{37}$$

remains negligible during a time propagation of $\Psi(t)$. In the present case we chose E_{cut} as 200 kcal/mol. Despite its simplicity, this procedure was found to reduce the half spectral range ΔH from 750 to 500 kcal/mol, thus leading to a factor of 1/3 reduction of the whole numerical effort. Similar methods of energy cutoff have been employed in several previous papers.[30,31]

For the second issue concerning a single multiplication of the Hamiltonian, we take full advantage of the parallel supercomputer, Fujitsu VPP-800, consisting of a number of vector processors, and we use 40 processors in the present work. To parallelize the computer code we divide the full-dimensional wave function according to the scattering coordinate R, and hence each processor contains a portion of the complete wave function for 2 grid points of R. With this scheme a full-dimensional wave function needs only 60 Mbytes core memory on each processor, compared to the size of 2.4 Gbytes of the complete wave function. Note that the interprocessor communication occurs only for the kinetic energy operator for R in Eq. (2). In order to reduce the amount of data transfer associated with this operator, we utilize a truncated version of the sinc-DVR matrix that is obtained by letting the off-diagonal elements with $|i-j| > 8$ to be zero (i and j denotes indices for the R grid). This
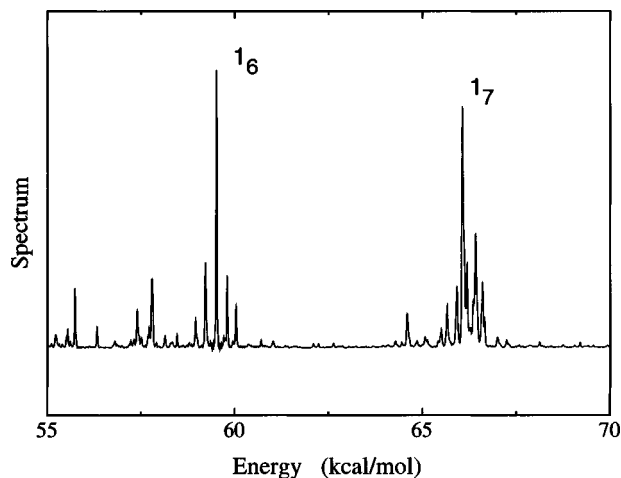
FIG. 2. Spectrum of the CH stretching source state obtained by Fourier transforming the autocorrelation function of this state. The zero of energy is set at the minimum of the potential surface of HFCO. The zeroth-order assignment, 1_n, represents that the mode 1 (CH stretch) is excited with n vibrational quanta.
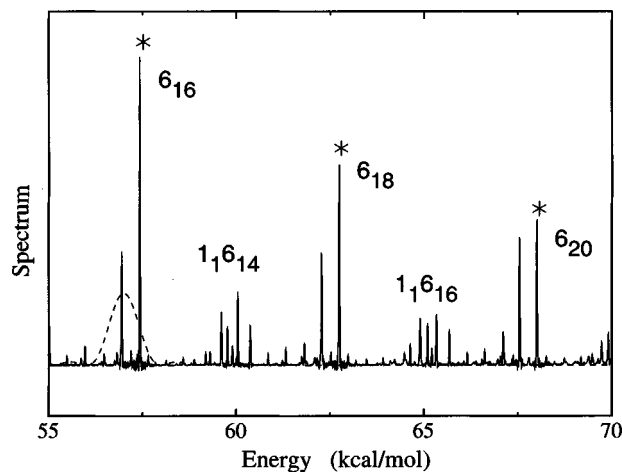

FIG. 3. Spectrum of the out-of-plane bending source state. The mode 6 denotes the out-of-plane bending mode. The square modulus of the filter function with window energy of 57 kcal/mol is depicted as a dashed curve (the height is scaled).

modification is essentially the same as using a 15-point numerical difference formula[32] and is useful to avoid all-to-all communication among processors. Since the parallel supercomputer used here provides the asynchronous communication mechanism that enables a simultaneous execution of computation and data transfer, essentially no extra CPU cost is required for data transfer itself as long as the time required for communication does not exceed that for computation. This feature leads to a nearly linear scaling with the number of processors, and in fact an approximately 200 Gflops rate on average is achieved in the present calculation (in other words, each vector processor runs with 5 Gflops). Also, it takes about 40 CPU hours to propagate a wave packet for 3 ps. Since each processor has a relatively large memory of 7 Gbytes, all filter states are stored directly on the core memory, which permits an explicit analysis of the constructed filter states.

III. RESULTS AND DISCUSSION

A. Assignment of spectral peaks

Employing the aforementioned method we propagated the two source vibrational states in Eqs. (26) and (28) up to 3 ps. Spectra of these states, or square modulus of the overlap with molecular eigenstates, were calculated by Fourier transforming the autocorrelation functions in Eq. (25). Figure 2 displays the spectrum of the CH stretching source state, Φ_{CH}, where we can see two clumps of peaks corresponding to the overtone states with $v = 6$ and 7. Since the dissociation threshold is 60.9 kcal/mol in the present potential surface, the overtone states for $v = 6$ and 7 are located just below and well above the dissociation threshold. We also show in Fig. 3 the spectrum of the out-of-plane bending source state, Φ_{OP}, where three clumps of highest peaks along with two clumps with moderate heights can be seen. We found that the former highest peaks correspond to the extreme-motion states that are assigned to 6_{16}, 6_{18}, and 6_{20}, respectively, while the latter moderate peaks have the character of $1_1 6_{14}$ and $1_1 6_{16}$

vibrational states. (Note that modes 1 and 6 denote the CH stretching and out-of-plane bending modes, respectively, and 6_{14} represents a state with 14 quanta in the mode 6.) Since these assignments are not trivial, we first describe a means of assignment in some detail.

Since full-dimensional wave functions of the individual molecular eigenstates are not available in this work, it is not possible to make an assignment by inspecting the nodal pattern of the wave functions. Therefore, a means of assignment not explicitly relying on the full-dimensional eigenstates is required. Here we utilized the fact that the motion of the H atom can be approximately described by using only r_2, θ_2, and ϕ degrees of freedom, and obtained information on the spectral peaks in Figs. 2 and 3 by analyzing the eigenstates of a subsystem describing the CH chromophore. First, we defined a 3D CH chromophore Hamiltonian by fixing the other Jacobi coordinates at their equilibrium values of HFCO in the total Hamiltonian as

$$\hat{H}^{3D} = -\frac{1}{2\mu_2}\frac{\partial^2}{\partial r_2^2} - \frac{1}{2I_2(r_2,\bar{\bar{R}})}\hat{D}(\theta_2)$$

$$- \frac{1}{2I(\bar{r}_1,r_2,\bar{R},\bar{\theta}_1,\theta_2)}\hat{D}(\phi)$$

$$+ \frac{1}{\mu\bar{R}^2}\{\cot\bar{\theta}_1\hat{F}(\theta_2)\hat{F}(\phi) + \cot\bar{\theta}_1\cot\theta_2\hat{G}(\phi)\}$$

$$+ V(\bar{r}_1,r_2,\bar{R},\bar{\theta}_1,\theta_2,\phi). \tag{38}$$

Eigenstates of this Hamiltonian, Φ_n^{3D}, were obtained by a direct diagonalization with the same PODVR bases. Next, we generated the following reduced source state:

$$\Phi_{OP}^{3D} = N\left(\sum_n \varphi_n^{(6)}(\phi)\right)\varphi_0^{(2)}(r_2)\varphi_0^{(5)}(\theta_2), \tag{39}$$

which was derived from the original source state Φ_{OP} by discarding the 1D vibrational functions for the fixed coordinates. Expanding the reduced source state in terms of the 3D chromophore eigenstates, Φ_n^{3D}, we obtained a stick spectrum
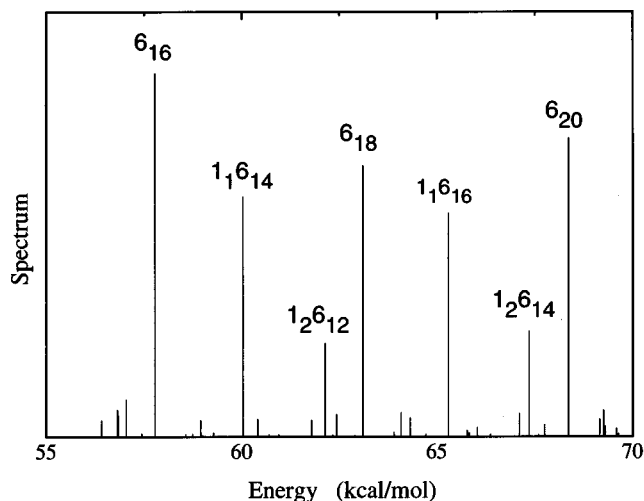
FIG. 4. Spectrum of the reduced out-of-plane source state obtained as the square modulus of overlap with the 3D chromophore eigenstates. The abscissa is the chromophore eigenenergy plus the zero-point energy for the fixed Jacobi coordinates.

in Fig. 4, which displays the distribution of overlap modulus squared, $|\langle \Phi_n^{3D} | \Phi_{OP}^{3D} \rangle|^2$, versus the 3D chromophore eigenenergy plus the zero-point energy for the fixed coordinates. By comparing this stick spectrum with the original spectrum in Fig. 3, we find that clear correspondence of peaks exists between these spectra. In fact, the reduced spectrum in Fig. 4 can be regarded as a zeroth-order approximation to the full-dimensional case in Fig. 3, and each stick peak in the former splits into many peaks in the latter due to the interaction between the CH chromophore and the remaining bath modes. Interestingly, the extent of state mixing, or splitting of the individual stick peaks, is significantly different between 6_{2m} and $1_1 6_{2m-2}$ bands; the latter bands suffer more strongly the effect of state mixing with the bath modes than the former, which indicates much stronger couplings among the in-plane vibrational modes. Figure 5 illustrates several 2D sections of the 3D wave functions corresponding to the strong stick
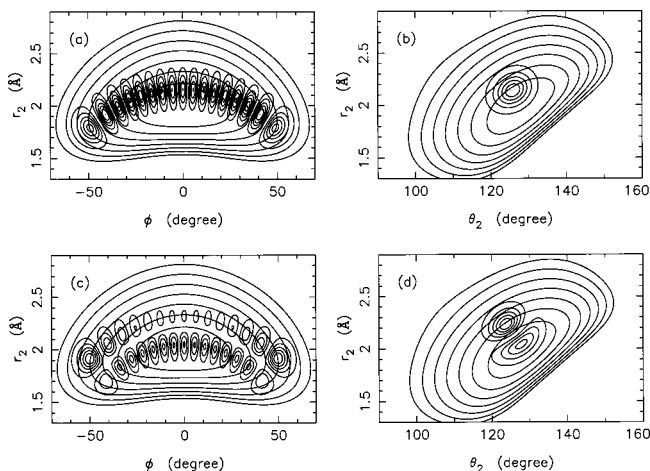

FIG. 5. Plots of the CH chromophore eigenstates: (a) and (b) correspond to the 6_{16} state, while (c) and (d) represent the $1_1 6_{14}$ state. The contour lines of the potential surface are with the spacing of 10 kcal/mol, from 10 to 70 kcal/mol.

TABLE II. A comparison of the energies and dissociation rates of the out-of-plane extreme-motion states. The calculated energies and rates correspond to the center of peaks indicated by asterisks in Fig. 3 and the time average of $k(t|E)$ over $t = 1-3$ ps in Fig. 7, respectively. The experimental values are taken from Ref. 5(c).

| | E (kcal/mol) | | $\log[k(\mathrm{s}^{-1})]$ | |
Assignment	Calc.	Expt.	Calc.	Expt.
6_{16}	57.4	57.4	7.9	$\leqslant 5.70$
6_{18}	62.7	62.6	9.0	$\geqslant 8.70$
6_{20}	68.0	67.8	9.8	9.84

peaks in Fig. 4. From the nodal patterns we can assign the stick peaks as 6_{2m}, $1_1 6_{2m-2}$, and $1_2 6_{2m-4}$, respectively, and thus these assignments are given to the original spectrum in Fig. 3. The energies of 6_{2m} peaks that are indicated by asterisks in Fig. 3 are listed in Table II, which shows that the agreement between these energies and the experimentally observed band origins is very good, especially considering the accuracy of the potential function used. We think that this agreement supports the validity of the procedure for the assignment employed here. We also applied a similar procedure to the CH stretching source state and assigned the two clumps of peaks in Fig. 2 as $v = 6$ and 7 by actually inspecting the relevant 3D wave functions.

B. Dissociation rates

We now discuss the results obtained for the individual filter states. In order to examine the dissociation dynamics at different energies, we applied a set of filter operators with different window energies, $\{\hat{F}_{T_0}(E_k)\}$, onto a single source state, thus generating the same number of filter states. The window energies $\{E_k\}$ were located over the energy range of 55–70 kcal/mol with equal spacings of 1 kcal/mol. The role of the filter operator can be schematically viewed by plotting the square modulus of the following filter function:

$$f_{T_0}(E; E_k) = \frac{\exp[i(E_k - E)T_0] - 1}{i(E_k - E)}, \qquad (40)$$

which is obtained by replacing the ABC Hamiltonian $\hat{H}_c$ with a real energy E in Eq. (13). One example of the filter function with $E_k = 57$ kcal/mol is plotted as a dashed curve in Fig. 3. We define the filter width, ΔE, as the spacing between the two zeros of $|f_{T_0}(E; E_k)|$ nearest to E_k, thus it becomes $4\pi/T_0$. Practically, the choice of ΔE or T_0 remains somewhat arbitrary, and in the present case we chose T_0 as 4000 a.u. $\simeq$ 100 fs so that ΔE became about 2 kcal/mol (this width is the same as that used in the previous work[21]).

We defined the survival and dissociation probability of each filter state as

$$P_s(t|E_k) = |\langle \Psi(t|E_k) | \Psi(t|E_k) \rangle|^2,$$

$$P_d(t|E_k) = 1 - P_s(t|E_k),$$

where $\Psi(t|E_k)$ denotes a filter state in Eq. (14). The variation of $P_d(t|E)$ vs E is plotted for $t = 1.0$, 1.5, 2.0, 2.5, and 3.0 ps in Fig. 6, which shows a monotonic increase of the
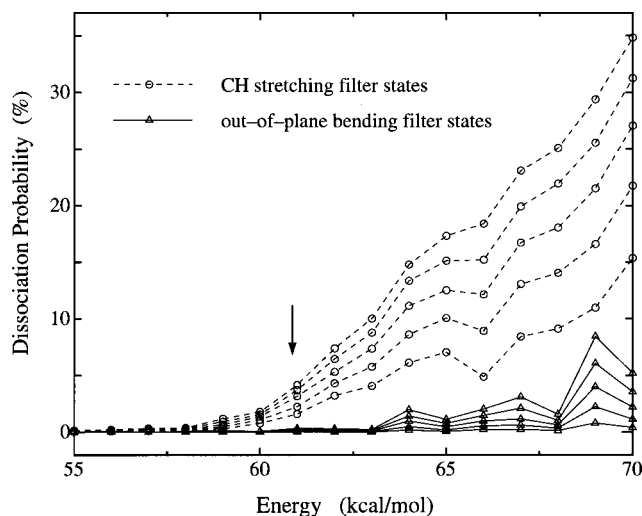
FIG. 6. The dissociation probability $P_d(t|E)$ as a function of window energy E. Circles and triangles represent the CH stretching and out-of-plane bending filter states, respectively. The curves are plotted for $t = 1.0$, 1.5, 2.0, 2.5, and 3.0 ps. The dissociation probability increases monotonically with time. The arrow indicates the dissociation threshold (60.9 kcal/mol).

dissociation probability with time. Also, the dissociation threshold is marked by the arrow. Figure 6 clearly indicates that the dissociation of the out-of-plane bending filter states, $\Psi_{OP}(t|E)$, is much slower than that of the CH stretching filter states, $\Psi_{CH}(t|E)$. For example, $P_d(t|E)$ for the out-of-plane case with $E = 68$ kcal/mol (which corresponds to the 6_{20} band in Fig. 3) is only 2% at $t = 3$ ps, while that of the CH stretching case already amounts to 25% at the same time. Also, at the window energy of 63 kcal/mol corresponding to the 6_{18} band, $\Psi_{OP}(t|E)$ exhibits almost no dissociation, but $\Psi_{CH}(t|E)$ dissociates by more than 10% at $t = 3$ ps. A similar comparison for the 6_{16} band at $E = 57$ kcal/mol is difficult with this figure, since the corresponding filter states are located deep in the tunneling region and thus essentially no dissociation occurs for those states.

The difference in the dissociation rates can be more clearly seen by examining the time-dependent decay coefficient, $k(t|E_k)$, defined by

$$\frac{d}{dt}P_s(t|E_k) = -k(t|E_k)P_s(t|E_k).\qquad(41)$$

Since $P_s(t|E_k)$ is available only at discrete times, $t = mT_0$ ($m = 0,1,2,...$), we evaluate $k(t|E_k)$ approximately using a finite difference scheme as

$$k\left(\left(m+\frac{1}{2}\right)T_0\bigg|E_k\right) \simeq -\frac{2}{P_{m+1,k}+P_{m,k}}\times\frac{P_{m+1,k}-P_{m,k}}{T_0},$$
$$(42)$$

where $P_{m,k}$ is the abbreviation of $P_s(mT_0|E_k)$. We show in Fig. 7 the time variation of $k(t|E)$ for fixed energies corresponding to the 1_n and 6_{2m} states. It is seen from this figure that the decay rates $k(t|E)$ for the 1_6 and 1_7 states increase rapidly within 0.5 ps and subsequently fluctuate around their asymptotic values. As discussed in the previous paper,[21] this behavior of $k(t|E)$ comes from the fast energy exchange between the in-plane CH stretch and bend through a strong

Fermi resonance, followed by slower energy redistribution into the remaining bath modes. For the 6_{2m} filter states, the decay rates exhibit a gradual increase over the entire time, which reflects a much slower energy transfer from the initial out-of-plane excitation into the other in-plane vibrational modes.

Figure 8 displays the time average of $k(t|E)$ over $t = 1-3$ ps [denoted as $\bar{k}(E)$] as a function of window energy E. The RRKM rate with tunneling correction[33,34] is also shown as a solid curve. We first confine attention to the rates above the dissociation threshold. The time-averaged rate $\bar{k}(E)$ for the 1_7 state ($\sim 10^{10.9}$) is in good agreement with the RRKM rate ($\sim 10^{10.8}$). In fact, $\bar{k}(E)$ for all the CH stretching filter states above the dissociation threshold are close to the RRKM estimates, indicating that the dissociation of those
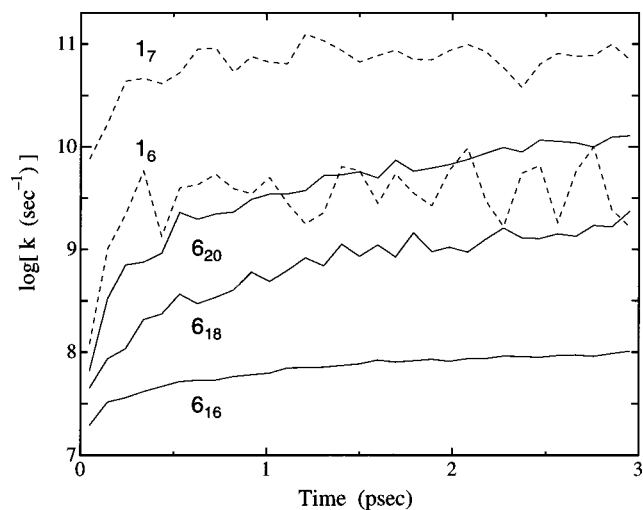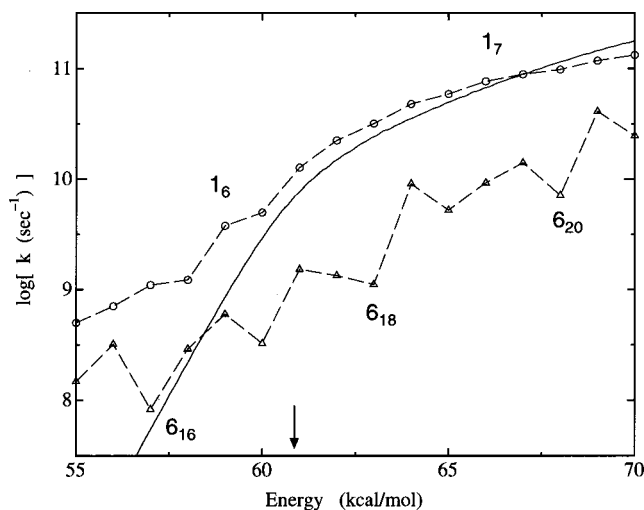

FIG. 7. The decay rate $k(t|E)$ as a function of time t. The window energy E is fixed at 57, 63, and 68 kcal/mol for the out-of-plane bending filter states (solid curves) and 59 and 66 kcal/mol for the CH stretching filter states (dashed curves), respectively.

FIG. 8. The time-averaged decay rate $\bar{k}(E)$ as a function of window energy E. $\bar{k}(E)$ is a time average of $k(t|E)$ over $t = 1-3$ ps. Circles and triangles represent the CH stretching and out-of-plane bending filter states, respectively. The RRKM rate with tunneling correction is shown by the solid curve. The dissociation threshold is marked by the arrow.

states can be well characterized by statistical theories. On the other hand, the averaged decay rates of the 6_{18} and 6_{20} states are about one order of magnitude smaller than those of the CH stretching filter states or the RRKM rates. This difference of rates should not be regarded simply as apparent non-RRKM behavior arising from the different initial distribution of vibrational energy,[33] since the growth of the rates for the 6_{2m} states in Fig. 7 is extremely slow as compared to the case of initial in-plane excitations studied here and in the previous work.[21] Also, as will be shown by a local-mode analysis below, the initial out-of-plane vibration of 6_{2m} states relaxes only slightly within 3 ps. These features clearly indicate that the couplings between the out-of-plane excited states and other in-plane vibrational states are weak, which is in qualitative agreement with the experimental findings.

We compare in Table II the time-averaged decay rates of 6_{2m} states with the experimental values.[9] The calculated rates for 6_{18} and 6_{20} states are in good agreement with the experimental ones, but that for 6_{16} state is greatly overestimated by two or more orders of magnitude than the experimental one. In addition, $\bar{k}(E)$ for the CH stretching filter states in Fig. 8 deviates significantly from the RRKM rates below the dissociation threshold. Hence, it is found that the calculated decay rates are larger than the RRKM estimates in the entire tunneling region regardless of the source states. This is not an artifact coming from insufficient accuracy of the Chebyshev expansion in Eq. (17), which was confirmed by changing the expansion order N_H or the parameters in the damping function. One of the possible reasons for this is the deficiency of the potential function; since the dissociation in this energy region is dominated by penetration of tails of a wave packet through the barrier, the decay rates are very sensitive to the accuracy of the potential function around the barrier. Another reason may be that a small amount of high energy components included in each filter state make the decay rates larger, which is possible because the magnitude of the filter function in Eq. (40) decays only algebraically as $E - E_k$ is increased.

Finally, we show the result of a local-mode analysis. We consider here the average vibrational energy in the out-of-plane bending and CO stretching modes, which is computationally convenient because these modes are well characterized by ϕ and r_1 of the Jacobi coordinates and hence all the calculations can be done within this coordinate system. The out-of-plane vibrational energy, $E_{\text{vib}}^{\text{OP}}$, is defined as a weighted average of eigenenergies of the 1D diabatic Hamiltonian $\hat{h}_6^{\text{dia}}$ in Eq. (27):

$$E_{\text{vib}}^{\text{OP}}(t|E_k) = \sum_n \epsilon_n^{(6)} P_n^{(6)}(t|E_k), \tag{43}$$

where $P_n^{(6)}(t|E_k)$ represents a probability for finding the nth eigenstate of $\hat{h}_6^{\text{dia}}$ in a filter state $\Psi(t|E_k)$, that is:

$$P_n^{(6)}(t|E_k) = \sum_{I'} |\langle i_{r_1}|\langle i_{r_2}|\langle i_R|\langle i_{\theta_1}|\langle i_{\theta_2}|\langle \varphi_n^{(6)}| \cdot |\Psi(t|E_k)\rangle|^2, \tag{44}$$

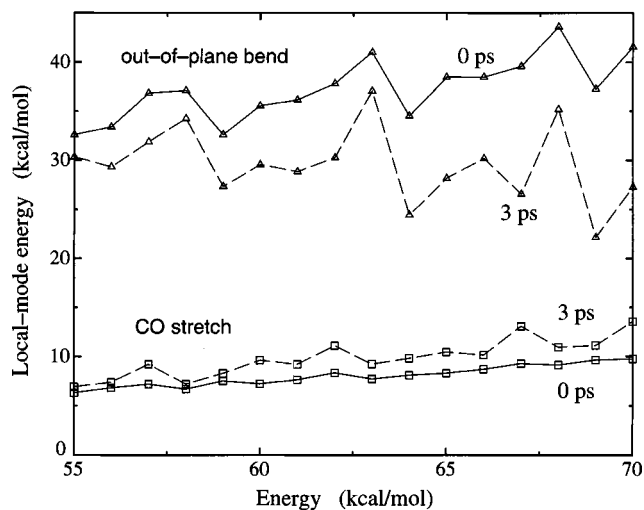where I' denotes the five indices of PODVR bases collec-

FIG. 9. The local-mode vibrational energy versus window energy E obtained for the out-of-plane bending filter states. Solid and dashed lines indicate the local-mode energy at $t = 0$ and 3 ps, while triangles and squares represent the out-of-plane bending and CO stretching energies, respectively.

tively. Since the norm of the filter state decreases with time, appropriate normalization is applied to the probabilities $\{P_n^{(6)}(t|E_k)\}$. The CO stretching energy, $E_{\text{vib}}^{\text{CO}}$, is also defined in a similar manner. Figure 9 shows the local-mode energies of the out-of-plane filter states at $t = 0$ and 3 ps. It is seen from this figure that $E_{\text{vib}}^{\text{OP}}$ for 6_{2m} states at $E = 57$, 63, and 68 kcal/mol remain more than 30 kcal/mol even at $t = 3$ ps, which indicates the stability of these states against IVR. This slow IVR contrasts well with the fast IVR initiated from the CH stretching excitation that proceeds considerably within 3 ps.[21]

Although all the filter states exhibit a large out-of-plane vibrational energy in Fig. 9, the degree of excitation differs according to the window energy. As expected from the spectral assignment in Fig. 3, $E_{\text{vib}}^{\text{OP}}$ for the 6_{2m} states exhibit the largest values, and those at $E \simeq 60$ and 65 kcal/mol corresponding to the $1_1 6_{2m-2}$ states are the second largest. For the window energy at which there are only small peaks in Fig. 3, e.g., at $E = 59$ or 64 kcal/mol, $E_{\text{vib}}^{\text{OP}}$ is further decreased, and hence the corresponding filter states are more excited in the in-plane modes. These differences of out-of-plane excitation in the filter states seem to cause the oscillation of $k(t|E)$ in Fig. 8, since the dissociation becomes faster if the initial in-plane excitation is larger. [Note in passing that $k(t|E)$ for the CH stretching case does not exhibit a similar oscillation in Fig. 8. Since there are energy regions where no strong peaks exist in Fig. 2, the filter states in these regions should be more or less excited in other vibrational modes. The decay rates of these states, however, become similar to the RRKM rates probably due to the strong couplings among the in-plane modes.] We also applied the local-mode analysis to the CH stretching filter states, and the energy transfer from the initially excited CH stretch to the out-of-plane bending or CO stretching modes was found to

proceed slowly within 3 ps, thus showing nonresonant IVR into these two modes.

IV. CONCLUSIONS

In this work we focused on comparing the dissociation rates of the out-of-plane bending or CH stretching excited states. Since the calculation of the individual molecular eigenstates near the dissociation threshold was computationally too expensive, we examined the relevant dynamical quantities by actually propagating the wave packets that were locally excited in a specific vibrational mode. A significant reduction of the computational effort became possible by using the commutation relation between the filter operator and the time evolution operator. The time-dependent decay coefficients of the filter states reflected the different types of underlying dynamics, and the slow IVR from the out-of-plane excitation was concluded by the decay rate constants as well as the local-mode analysis.

Hose and Taylor[35] discussed previously the origin of the stability of extreme-motion states against IVR from two different points of view: one is the effect of an adiabatic dynamical potential that decouples a highly excited mode from other vibrational modes, and the other is the smallness of the number of effective coupling elements between such an extreme-motion state with other zeroth-order states. Examples of such extreme-motion states may include highly excited SO stretching states of the SO_2 molecule[36,37] and the bending excited states in acetylene,[38] both of which have been studied with an emphasis on the normal-to-local mode transition. An interesting question concerning these states is whether all vibrational modes have their corresponding extreme-motion states. In the case of HFCO, there remains a possibility that the in-plane vibrational modes show such states, but the study of this problem would require the quantum mechanical calculation of all the molecular eigenstates near the dissociation threshold. Once these eigenstates are explicitly calculated, the correlation between the state-resolved decay rates and the vibrational character of each eigenstate could be analyzed, which would yield crucial information on how a statistical dissociation or IVR is realized from the set of resonance states. It is also of interest to study the rotational effect on the dissociation rates that is known to be dramatical in HFCO.[9] All of these remain a challenge for future work.

ACKNOWLEDGMENTS

[1] *Dynamics of Molecules and Chemical Reactions*, edited by R. E. Wyatt and J. Z. H. Zhang (Marcel Dekker, New York, 1996).

[2] J. Z. H. Zhang, *Theory and Application of Quantum Molecular Dynamics* (World Scientific, Singapore, 1999).

[3] M. F. Herman and E. Kluk, Chem. Phys. **91**, 27 (1984).

[4] V. S. Batista and W. H. Miller, J. Chem. Phys. **108**, 498 (1998); X. Sun and W. H. Miller, *ibid.* **110**, 6635 (1999).

[5] Y. Elran and K. G. Kay, J. Chem. Phys. **110**, 3653 (1999).

[6] F. S. Mayor, A. Askar, and H. A. Rabitz, J. Chem. Phys. **111**, 2423 (1999).

[7] R. E. Wyatt, J. Chem. Phys. **111**, 4406 (1999).

[8] U. Manthe, H. D. Meyer, and L. S. Cederbaum, J. Chem. Phys. **97**, 3199 (1992); F. Matzkies and U. Manthe, *ibid.* **108**, 4828 (1998), and references therein.

[9] (a) Y. S. Choi and C. B. Moore, J. Chem. Phys. **90**, 3875 (1989); (b) **94**, 5414 (1991); (c) **97**, 1010 (1992); (d) **103**, 9981 (1995).

[10] J. C. Crane, A. Kawai, H. Nam, H. Clauberg, H. P. Beal, P. Guinn, and C. B. Moore, J. Mol. Spectrosc. **183**, 273 (1997); J. C. Crane, H. Nam, H. Clauberg, H. P. Beal, I. J. Kalinovski, R. G. Shu, and C. B. Moore, J. Phys. Chem. A **102**, 9433 (1998).

[11] K. Morokuma, S. Kato, and K. Hirao, J. Chem. Phys. **72**, 6800 (1980); K. Morokuma and S. Kato, in *Potential Energy Surfaces and Dynamics Calculations*, edited by D. G. Truhlar (Plenum, New York, 1981), p. 243.

[12] J. D. Goddard and H. F. Schaefer III, J. Chem. Phys. **93**, 4907 (1990).

[13] W. H. Green, D. Jayatilaka, A. Willetts, R. D. Amos, and N. C. Handy, J. Chem. Phys. **93**, 4965 (1990).

[14] K. Kamiya and K. Morokuma, J. Chem. Phys. **94**, 7287 (1991).

[15] J. S. Francisco and Y. Zhao, J. Chem. Phys. **96**, 7587 (1992).

[16] T-G. Wei and R. E. Wyatt, J. Phys. Chem. **97**, 13580 (1993).

[17] T. Yamamoto and S. Kato, J. Chem. Phys. **107**, 6114 (1997).

[18] F. E. Budenholzer and T. Yu, J. Phys. Chem. A **102**, 947 (1998).

[19] A. Viel and C. Leforestier, J. Chem. Phys. **112**, 1212 (2000).

[20] R. A. Friesner, J. Bently, M. Menou, and C. Leforestier, J. Chem. Phys. **99**, 324 (1993).

[21] T. Yamamoto and S. Kato, J. Chem. Phys., **109**, 9783 (1998).

[22] M. J. Bramley and T. Carrigton, Jr., J. Chem. Phys. **99**, 8519 (1993).

[23] J. Echave and D. C. Clary, Chem. Phys. Lett. **190**, 225 (1992).

[24] D. T. Colbert and W. H. Miller, J. Chem. Phys. **96**, 1982 (1992).

[25] S. Skokov, J. Qi, J. M. Bowman, C-Y. Yang, S. K. Gray, K. A. Peterson, and V. A. Mandelshtam, J. Chem. Phys. **109**, 10273 (1998).

[26] T. Seideman and W. H. Miller, J. Chem. Phys. **96**, 4412 (1992).

[27] V. A. Mandelshtam and H. S. Taylor, J. Chem. Phys. **103**, 2903 (1995).

[28] W. H. Press, S. A. Teukolsky, W. T. Vetterling, and B. P. Flannery, *Numerical Recipes in Fortran 77*, 2nd ed. (Cambridge University Press, Cambridge, 1996).

[29] N. C. Handy, Mol. Phys. **61**, 207 (1987).

[30] F. Göğtas, G. G. Balint-Kurti, and A. R. Offer, J. Chem. Phys. **104**, 7927 (1996).

[31] V. A. Mandelshtam and H. S. Taylor, J. Chem. Soc., Faraday Trans. **93**, 847 (1997).

[32] T. C. Germann and W. H. Miller, J. Phys. Chem. A **101**, 6358 (1997).

[33] T. Baer and W. L. Hase, *Unimolecular Reaction Dynamics* (Oxford University Press, Oxford, 1996).

[34] W. H. Miller, J. Am. Chem. Soc. **101**, 6810 (1979).

[35] G. Hose and H. S. Taylor, Chem. Phys. **84**, 375 (1984).

[36] T. Sako and K. Yamanouchi, Chem. Phys. Lett. **264**, 403 (1997).

[37] G. Ma and H. Guo, J. Chem. Phys. **111**, 4032 (1999).

[38] M. P. Jacobson, R. J. Silbey, and R. W. Field, J. Chem. Phys. **110**, 845 (1999).